

**Comparison of Perovskite and Perovskite Derivatives for
use in Anion-based Pseudocapacitor Applications**

Journal:	<i>Journal of Materials Chemistry A</i>
Manuscript ID	TA-ART-06-2019-006094.R1
Article Type:	Paper
Date Submitted by the Author:	22-Jul-2019
Complete List of Authors:	Forslund, Robin; University of Texas at Austin, Chemistry Pender, Joshua; University of Texas at Austin, Department of Chemistry Alexander, Caleb; University of Texas at Austin, Chemical Engineering Johnston, Keith; University of Texas at Austin, Department of Chemical Engineering Stevenson, Keith; Skolkovo Institute of Science and Technology,

ARTICLE

Comparison of Perovskite and Perovskite Derivatives for use in Anion-based Pseudocapacitor Applications

Robin P. Forslund,^a Joshua Pender,^a Caleb T. Alexander,^b Keith P. Johnston,² and Keith J. Stevenson*^c

Received 00th January 20xx,
Accepted 00th January 20xx

DOI: 10.1039/x0xx00000x

The electrochemical behavior of perovskite oxides utilizing calcium and manganese along with their Ruddlesden-Popper (RP) counterparts are evaluated as anion intercalation-based pseudocapacitors by cyclic voltammetry and galvanostatic charging/discharging in 1 M KOH. We find that higher oxygen vacancy contents (δ) achieved by annealing in a reducing atmosphere leads to greater charge storage capacities. Additionally, we demonstrate how the governing descriptor for pseudocapacitive performance shifts from the number of oxygen vacancies and surface redox sites at high scan rates to facile oxygen diffusion and the ability to store oxide anions within interstitial sites of the rock salt layers in the RP materials at low scan rates. Both the perovskite and RP materials are evaluated as two-electrode asymmetric pseudocapacitors utilizing SrFeO_{2.5} as the anode material. The cell containing SrFeO_{2.5}/Ca₂MnO_{4.6} performed the best with a high energy density of 73 Wh kg⁻¹ at a power density of 530 W kg⁻¹.

Introduction

As the popularity and necessity of sustainable, renewable energy sources such as wind and solar continues to grow so too does the demand for new, efficient means of storing energy from these intermittent sources. While lithium ion batteries and fuel cells have proven to be effective means of storing electricity, they require extended charging and discharging time periods and fail to handle the rapid charging and discharging rate requirements mandated by the nature of these energy sources. On the other end of the spectrum, traditional electrostatic capacitors can deliver high power but at a significant cost to their energy densities. Electric double layer capacitors (EDLCs) that utilize high surface area carbons, known as supercapacitors, as well as metal-oxide based materials, known as pseudocapacitors, have shown great promise as an intermediary to bridge this gap in both energy and power densities.¹

In a parallel plate capacitor charge is stored non-faradaically as electrostatic charge via electric double layer formation. Devices known as electric double layer capacitors (EDLCs) utilize high surface area materials such as carbons with surface areas >1000 m² g⁻¹ as electrodes and rely on the concept of electric double layer capacitance to achieve over 300 F g⁻¹, however, these power densities come at a cost to the total energy density of the device.²

Pseudocapacitors bridge the gap between batteries and EDLCs in that in addition to any double layer capacitance, they store charge

by utilizing faradaic process involving surface or near surface redox reactions that give rise to capacitive electrochemical features.³ In addition to the classic rectangular capacitance envelope seen for EDLCs during cyclic voltammetry (CV) experiments, pseudocapacitors also display peaks that are indicative of redox processes within the electrode material, which means that the voltage-current response is not the same over the entire window. The energy density of a capacitor is given by:

$$E = \frac{1}{2}CV_{cell}^2 \quad (1)$$

where E is the energy density (Wh g⁻¹), C is the specific capacitance (F g⁻¹) of the electroactive material, and V_{cell} is the voltage applied to the entire cell.³

By replacing organic electrolytes with water we can utilize the entire pH range and a wide variety of solution ions such as H₂SO₄ at low pH, NaSO₄ around neutral pH, and NaOH and KOH in alkaline conditions.⁴ This change opens up the variety of materials that can be used such as oxides with MnO₂, NiO, Co₃O₄ and V₂O₅ having been recently studied along with numerous others.³⁻⁶ Given that the energy density goes as the square of the voltage window as shown above in Eq.1, one strategy to improve cell performance has been to utilize different materials at the two electrodes, such as TiO₂/MnO₂, supported on high surface area carbons to expand the voltage window.⁷

There are four generally proposed operational mechanisms of pseudocapacitance. The first is surface redox reactions that occur in materials such as metal oxides and hydroxides. For example, Ni(OH)₂ can be reversibly oxidized to NiOOH via deprotonation in basic electrolyte to store charge.^{8,9} The second mechanism of pseudocapacitive charge storage utilizes underpotential deposition and electrosorption such as in the case of proton underpotential deposition on Pt.^{10,11} The third and fourth mechanisms utilize rapid intercalation and deintercalation of ions into and out of the bulk material. For example, MoO₃ can be reversibly reduced and oxidized

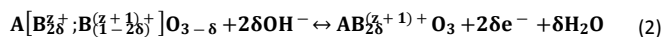
^a Department of Chemistry, The University of Texas at Austin, 1 University Station, Austin, Texas 78712, USA. Address here.

^b McKetta Department of Chemical Engineering, The University of Texas at Austin, 200 E Dean Keeton St., Austin, Texas 78712, USA.

^c Center for Energy Science and Technology, Skolkovo Institute of Science and Technology, Bolshoi Boulevard 30, Moscow 121205, Russia.

Electronic Supplementary Information (ESI) available: [details of any supplementary information available should be included here]. See DOI: 10.1039/x0xx00000x

to intercalate and to deintercalate cations such as H⁺ and Li⁺.^{12,13} As recently shown by Mefford et al. and Alexander et al., pseudocapacitive charge storage using anions (OH⁻) can be achieved with perovskites.^{13,14} Our group has shown that the anion intercalation mechanism is affected by the oxygen vacancy content (δ) and can be described in a perovskite for a given transition metal B as:



To put it simply, more oxygen vacancies present in the lattice means there are more empty sites for OH⁻ ions to fill and thus increase the amount of stored charge. It is this last type of mechanism of reversible anion based pseudocapacitive charge storage that we investigate herein.

Perovskite oxides have the formula ABO₃ where the A-site is typically made up of an alkaline earth or rare earth metal while the B-site is made up of one or more transition metals. Additionally, there are multiple derivatives of this structure including Ruddlesden-Popper (RP) oxides that have a crystal structure represented as A_{n+1}B_nO_{3n+1} or equivalently (AO)(ABO_{3±δ})_n, wherein *n* (BO₆) octahedra perovskite layers are separated by rocksalt (AO)(OA) double layers. Previous work by our group demonstrated how the perovskite LaMnO_{3-δ} utilized a newly described hydroxide intercalation mechanism to achieve impressive pseudocapacitive performance and how reduction of the bulk structure introduced oxygen vacancies that greatly improved the amount of charge that could be stored.¹⁴ An additional study of La_{1-x}Sr_xMO_{3-δ} (M = Mn, Fe, Co) perovskites demonstrated how increased oxygen vacancies upon substitution of La for Sr resulted in exceptional pseudocapacitive performance.¹⁵ Furthermore, we have demonstrated how increased M – O bond covalency in the perovskite La_{1-x}Sr_xCoO_{3-δ} and in Ruddlesden-Popper (RP) oxides with the formula La_{2-x}Sr_xNi_{1-y}Fe_yO_{4+δ}, a derivative of the perovskite structure, allowed for increased rates of oxygen diffusion. Oxygen diffusion through vacancies within the perovskite lattice or through the rock salt layer of the RP structure aided in the exceptional performance of these oxides towards the oxygen evolution reaction (OER)¹⁶ as well as the electrooxidations of urea and small alcohols.^{8,17} Elsewhere, others have demonstrated how perovskite materials can be used as anion-based pseudocapacitors with Ba_{1-x}Sr_xCo_{1-y}Fe_yO_{3-δ}, LaNiO₃, SrCo_{0.9}Nb_{0.1}O_{3-δ}, and La_{1-x}Ca_xMnO₃ proving to be some of the most effective compositions.¹⁸⁻²²

Herein, we report the synthesis and electrochemical evaluation of CaMnO_{3-δ} perovskite and Ca₂MnO_{4-δ} Ruddlesden-Popper materials as pseudocapacitor materials to leverage previously discovered trends in catalytic and capacitive activity to further the understanding of how complex metal oxides can be tuned to increase their ability to store charge via anion intercalation. The specific choice of Ca as the A-site element and Mn in the B-site was made based upon the ability to synthesize both perovskite and Ruddlesden-Popper versions of the same composition under the same conditions and the well-documented ability to introduce large numbers of oxygen vacancies into both structures.^{23,24} CaMnO₃ and its reduced counterpart have been well-studied for oxygen evolution and reduction,²⁵⁻²⁹ however, only once CaMnO₃ been studied as an electrochemical anion-based pseudocapacitor to our knowledge.²¹ Upon annealing of the as-synthesized materials in a reducing

atmosphere to introduce increased amounts of oxygen vacancies, both reduced materials displayed greater charge storage compared to their unreduced counterparts, demonstrating how greater oxygen vacancy concentrations within the bulk of these materials increases their ability to store charge via oxide anion-based intercalation. Furthermore, we demonstrate how the governing descriptor for pseudocapacitive performance changes from a dependence on the number of surface transition metal redox active sites and oxygen vacancies at fast charge/discharge rates versus at slower rates where improved oxygen diffusion through the bulk lattice dominates. Finally, we demonstrate how both materials may be implemented into an asymmetric pseudocapacitor cell utilizing both reduced manganese materials as cathodes and Brownmillerite SrFeO_{2.5} as the anode to achieve impressive performance at varying charge and discharge rates.

Experimental

Material Synthesis

All materials were synthesized using the same modified Pechini method utilized in our previous work.^{16,17} Precursor particles were synthesized by dissolving A and B-site nitrate salts in the appropriate stoichiometric ratios in water to make a solution with a total metal salt concentration of 0.1 M. Citric acid and ethylenediaminetetraacetic acid (EDTA) were added to the solution each at a molar ratio of 1:1 with the total metal nitrate salts. Tetramethylammonium hydroxide (TMAOH) was added to the solution until the pH reached 7.5 to ensure deprotonation of three of the four EDTA carboxylic acid groups and that it had completely dissolved. Diethylene glycol (DEG) was then added to the solution at a concentration of 0.067 M and the solution was heated to 85° C while stirring. When heated, a dehydration reaction between the polyhydroxyl alcohol and the carboxylic acid groups of the chelates formed a polyester gel. After complete evaporation of the water the gel was combusted at 350° C to form mixed metal oxide precursor particles. This step was performed on a hot plate and not in a sealed furnace to avoid possible explosions from rapid evolution of gasses upon combustion. Finally, precursor particles were crystallized at 950° C for 5 hours under pure O₂ flowing at 100 mL min⁻¹ in a tube furnace. Half of the resulting catalyst material was then annealed at 325° C for 2 hours under an atmosphere of 7% H₂ in Ar flowing at 50 mL min⁻¹ to reduce the active material and introduce oxygen vacancies. All catalysts were recovered and immediately stored under Ar gas to prevent possible catalyst surface amorphization.

Powder X-ray Diffraction (PXRD)

The crystal structures of all materials were probed by X-ray diffraction using a Rigaku MiniFlex600 Diffractometer utilizing Cu K α radiation (1.54 Å wavelength) and operating at 40 kV and 15 mA at 298 K in ambient conditions. For all tests oxide powder was scanned over 20 - 90° 2 θ in 0.1° increments with a dwell time of 0.2 seconds per step.

Surface Area Analysis

Nitrogen sorption analysis was performed on a Quantachrome Instruments NOVA 2000 high-speed surface area BET analyzer at a temperature of 77 K. Prior to measurements, the samples were ball

milled for three minutes followed by degassing in vacuum for 12 hours at 120° C. The specific surface area was calculated using the BET method from the nitrogen adsorption data in the relative pressure range (P/P_0) of 0.05 to 0.30, with a minimum R^2 of 0.995 and minimum C value of 20.

Scanning Electron Microscopy (SEM)

Samples were prepared by dispersing unsupported material in ethanol (0.1 mg mL⁻¹) and depositing drops of suspension onto silicon wafers which were dried at 85° C for 30 minutes. Images were taken on a Hitachi S5500 SEM using an accelerating voltage of 40 kV and probe current of 15 nA.

Iodometric Titrations

Iodometric titrations were performed by adding 3 mL of deoxygenated 2 M KI to a flask containing 15 – 20 mg of perovskite and the perovskite was dispersed for three minutes via sonication.¹³ Next, the dispersion was added to a flask containing 25 ml of deoxygenated 1 M HCl and the perovskite was allowed to dissolve under an argon atmosphere. After 10 minutes the solution was titrated to a faint golden color with a solution of ~25 mM solution of Na₂S₂O₃ that had been pre-standardized with 0.1 N KIO₃. Three drops of potato starch indicator was then added and the solution was titrated until it was clear and colorless, marking the end point. All measurements were performed in triplicate and all solutions were made using pre-boiled deionized water.

X-ray Photoelectron Spectroscopy (XPS)

Chemical states at the material surface were characterized by a Kratos AXIS Ultra DLD XPS in 0.1 eV steps using a dwell time of 4 s per step and a monochromatic Al X-ray source (Al α , 1.4866 eV). Charge neutralization was used for all samples. Binding energies for all spectra were calibrated against the adventitious carbon peak at 285 eV. CasaXPS was used for all data analysis and deconvolution.

Electrochemical Characterization

The catalysts and Vulcan carbon were each ball-milled for three minutes before being mixed together and ball milled again for three minutes in an 85:15 perovskite:carbon weight ratio. For three-electrode cell measurements catalyst inks were prepared by adding 3 mL of a NaOH neutralized 0.05 wt% Nafion solution in ethanol to 3 mg of catalyst powder (1 mg mL⁻¹) and bath sonicated for 45 minutes. 10 μ L of ink was drop cast onto a clean 5 mm (0.196 cm², Pine Instruments) glassy carbon electrode and dried under ambient conditions overnight. Glassy carbon electrodes were cleaned prior to drop casting by sonication in a 1:1 by volume DI water:ethanol solution. Electrodes were then polished using 0.05 μ m alumina powder on a polishing pad, rinsed with DI water, sonicated in a fresh DI water:ethanol solution, and rinsed with DI water again before being dried in ambient air. All electrodes were prepared this way to obtain a composite catalyst loading of 51 μ g_{total} cm⁻², yielding 43.3 μ g_{oxide} cm⁻² and all three-electrode electrochemical tests were performed on electrodes prepared this way. Electrochemical testing was performed on a Metrohm Autolab PGSTAT302N potentiostat equipped with high speed rotators from Pine Instruments. All testing was performed at room temperature in Ar-saturated 1 M KOH (measured pH \approx 13.7). Positive feedback methods were used to determine electrolyte resistance (6 Ω) and all data was iR

compensated after testing unless stated otherwise. Each rotating disk electrode (RDE) test was performed in a standard three-electrode cell using a CH Instruments Hg/HgO (1 M KOH) reference electrode, a fritted Au wire counter electrode, and a film of catalyst ink on glassy carbon as the working electrode. All potentials are reported versus the Hg/HgO (1 M KOH) reference electrode. Materials were cycled three times at 10 mV s⁻¹ prior to testing to ensure stable spectra were being collected. Specific capacitances (F g⁻¹) were calculated from CVs according to equation 3:

$$C_s = \frac{1}{2mv|v_c - v_a|} \int_{V_a}^{V_c} i(V) dV \quad (3)$$

where m is the mass loading of electroactive material on the electrode (g), v is the potential scan rate of the CV (V s⁻¹) while V_c and V_a are the cathodic and anodic limits of the CV window.³ The integral represents the entire area within the CV loop over the cathodic and anodic sweeps which is divided by 2 to yield the average capacitance for a single sweep. Electrodes for every sample were tested at each scan rate (100, 50, 25, 10, 5 mV s⁻¹) with each electrode's capacitance measured in triplicate on separate electrodes to get an average and standard deviation.

Asymmetric, two-electrode cell tests were performed by supporting the catalyst/carbon composite on carbon fiber paper (CFP) electrodes measuring 1 cm². The CFP electrodes were prepared by rinsing in acetone for 10 minutes followed by exposure to 3 M nitric acid for 30 seconds, neutralization in a saturated solution of sodium bicarbonate, and rinsing in ethanol and then water. An ink containing 10 mg of catalyst composite per mL of ethanol was drop cast onto the prepared CFP electrodes to achieve a mass loading of 1 mg cm⁻².

Results and Discussion

CaMnO₃²⁰ and Ca₂MnO₄²⁰ materials were synthesized using a modified Pechini method as described above followed by calcination at 950° C to yield a phase-pure orthorhombic perovskite and $n = 1$ Ruddlesden-Popper (RP) structures as confirmed by powder X-ray diffraction (Figure 1a).²³ Precursor particles measuring between 50 nm and 150 nm sintered during calcination at high temperature to form larger particles ranging from 200 nm up to microns in diameter as shown by SEM (Figure 1b). BET surface areas for the perovskite and Ruddlesden-Popper samples were measured to be 4.5 m² g⁻¹ and 6.2 m² g⁻¹, respectively (Figure S1). Between the similarities in particle morphology seen using SEM and the similar BET surface areas we can confirm that both samples have approximately the same morphology, a characteristic that is important in order to reliably compare the electrochemical properties of multiple materials. Additional SEM images of the as-synthesized perovskite and RP materials can be found in Figures S2 and S3.

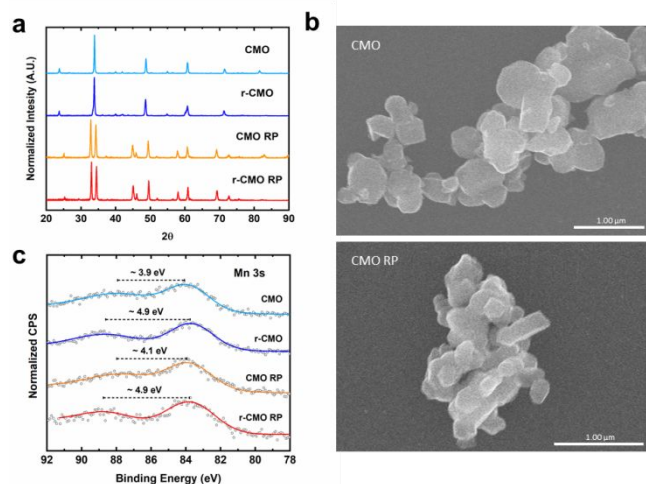


Figure 1: Physical characterization of CaMnO_3 (CMO) and $\text{Ca}_2\text{MnO}_{4-6}$ (CMO RP) materials. (a) PXRD patterns of as-synthesized CMO and CMO RP and reduced r-CMO and r-CMO RP materials. (b) SEM images of CMO and CMO RP indicating similar particle morphologies. (c) Deconvoluted Mn 3s XPS spectra for CMO, CMO RP, r-CMO and r-CMO RP.

Half of the material from each sample was reduced in an atmosphere of 7% H_2 in Ar at 325° C as has been previously reported²³ and iodometric titrations were performed on all four materials to determine the bulk oxygen content and average B-site oxidation state in both the as-synthesized and reduced samples for each crystal structure. For simplicity we will refer to the as-synthesized, more-oxidized CaMnO_3 as CMO and the reduced version as r-CMO while the oxidized Ruddlesden-Popper will be referred to as CMO RP and the reduced version will be referred to as r-CMO RP. Results of the iodometric titrations are given in Table 1. Reduction resulted in increased oxygen vacancy contents and, correspondingly, decreased Mn oxidation states for both the perovskite and RP crystal structures. Interestingly, with an average oxidation state of 4.22 in CMO, the material is found to contain a small amount of Mn^{5+} which is rarely seen. XPS measurements of all four samples corroborate the results of the iodometric titrations in that the surface oxidation states of both the perovskite and RP materials decreased after reduction (Figures 1, S4, Table 1) Investigation of the Mn 3s spectra shows a peak splitting in CMO of ~3.9 eV which indicates an approximate oxidation state of Mn slightly above 4+ while the splitting of these peaks for the other three CMO materials is between 4 eV and 5 eV, indicating oxidation states between 3+ and 4+.³⁰ Past work using employing thermodynamic calculations showed how increased partial pressures of oxygen at 950° C, the calcination temperature we used, resulted in fewer oxygen vacancies and that this trend approached a complete lack of oxygen vacancies in a purely oxygen atmosphere,³¹ the same as with our synthesis. This makes sense as more oxygen present in the atmosphere during synthesis should result in a greater amount of oxygen in the bulk material. As for the excess oxygen present in the lattice of CMO, we have observed this before in previous work on $\text{LaMnO}_{3.09}$ as a pseudocapacitor¹⁴ as well as in RP oxides used for the

OER,¹⁶ so this observation is not without precedent. Furthermore, the reduced versions of both the CMO and the CMO RP materials display greater splitting than their unreduced counterparts, qualitatively confirming the reduction of Mn and the introduction of oxygen vacancies. Integration of the Mn 2p 3/2 and 5/2 peaks show a decrease in Mn oxidation state in both the perovskite and RP samples, and the ratios of Ca to Mn were consistent with formation of either the perovskite or RP structure for all four samples (Table 1, Figure S4). It is widely accepted that for materials of the same crystal structure, such as perovskites, greater numbers of oxygen vacancies within the bulk directly correlate with increased oxygen intercalation and capacitance. With that in mind, for perovskite oxides the crystal structure often becomes unstable when more than 1/6 of the oxygen is removed, and our attempts to introduce greater amounts of vacancies by using higher temperatures during reduction resulted in phase impurities. Thus it is rational to conclude that the optimum δ for both the materials is 0.5.

Table 1: Physical characterization of CaMnO_{3-x} and $\text{Ca}_2\text{MnO}_{4-x}$

Sample	Composition	B^{AVG} (Iodometry)	Oxygen Vacancy Content (δ)	Mn 3s Splitting (XPS)	B^{AVG} (XPS)	Ratio of Ca/Mn (XPS)
CMO	$\text{CaMnO}_{3.11}$	4.22 ± 0.006	-0.11 ± 0.003	~3.9 eV	4.0	1.05
r-CMO	$\text{CaMnO}_{2.53}$	3.06 ± 0.011	0.47 ± 0.005	~4.9 eV	3.2	1.08
CMO RP	$\text{Ca}_2\text{MnO}_{3.92}$	3.85 ± 0.012	0.08 ± 0.008	~4.1 eV	3.9	1.8
r-CMO RP	$\text{Ca}_2\text{MnO}_{3.61}$	3.23 ± 0.011	0.39 ± 0.005	~4.9 eV	3.2	1.9

Electrochemical Characterization

The pseudocapacitance of all four samples was first characterized using cyclic voltammetry in Ar-saturated 1 M KOH and all samples were supported at 85 wt% on Vulcan carbon XC-72 (VC). A carbon support is used because when drop cast the unsupported material particles only contact each other and the GCE surface through point contacts. By supporting the oxide materials on VC the electrical contact resistances between adjacent catalyst particles are minimized and better conductivity between the GCE electrode and the catalyst is achieved. Furthermore, we use VC for these studies because it is a relatively low surface area carbon, which minimizes the contribution to the overall capacitance from charging of an electrochemical double layer, and also because it lacks surface functionalities that may interact with and significantly alter the electronic structure of the oxide material. This allows us to be confident that the differences in pseudocapacitive performance across the oxide materials we examined are due to differences in the metal oxides themselves. Low mass loadings of 51 $\mu\text{g}_{\text{total}} \text{cm}^{-2}$ were used to ensure efficient material utilization which allows for more detailed study of charge storage mechanisms.

Figure 2 shows CVs performed at varying scan rates for r-CMO and r-CMO RP and Figure S5 shows CVs at multiple scan rates for the unreduced samples. A pair of features are seen on the anodic scan at low scan rates for all four samples with a sharp peak appearing near -0.07 V vs. Hg/HgO (1 M KOH) at 5 mV s^{-1} along with a lesser peak at -0.25 V, characteristic of $\text{Mn}^{3+/4+}$ and $\text{Mn}^{2+/3+}$ redox reactions, respectively¹⁴ and at faster scan rates the feature at -0.25 V becomes indiscernible from the background current. Two peaks are observed on the cathodic scan for each sample as well that correspond to the

reverse redox reactions mentioned above. While the average Mn oxidation states for all four samples are above 3+ (Table 1), it is well documented that CaMnO_3 has low electrical conductivity and it is possible that without itinerant electron behavior, localized regions of more-reduced Mn may exist due to the dissociation of Mn^{3+} into Mn^{2+} and Mn^{4+} .²⁸

As can be seen in Figure 2, the gravimetric capacitances of both the perovskite and the Ruddlesden-Popper increase with the introduction of (more) oxygen vacancies. Interestingly, at high scan rates the measured capacitance of r-CMO is significantly greater than that of r-CMO RP while this trend reverses at low scan rates. For the unreduced samples, the gravimetric capacitances of the two different crystal structures are approximately the same at high scan rates, but at low scan rates CMO RP displays a much higher pseudocapacitance than CMO and approaches that of its reduced counterpart. When CVs are performed at 100 mV s^{-1} , the resulting capacitance values increase almost linearly with oxygen vacancy concentration across all four samples. While CVs that are performed at 5 mV s^{-1} also show a mild dependence on oxygen vacancy concentration, this relationship is somewhat muted and r-CMO RP stores the greatest amount of charge despite having fewer oxygen vacancies than its perovskite counterpart.

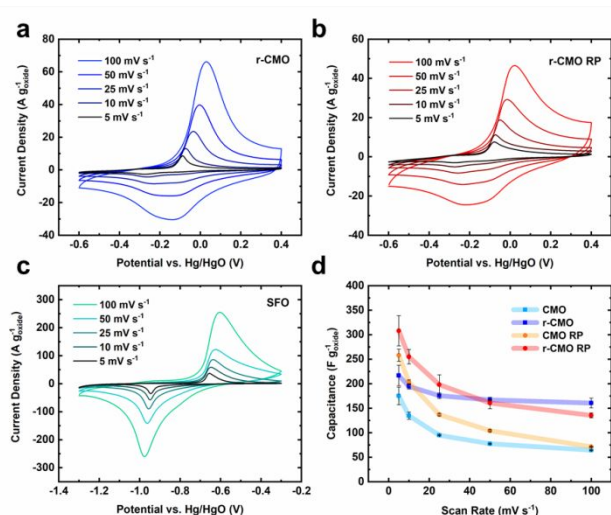


Figure 2: Electrochemical characterization of CaMnO_3 and Ca_2MnO_4 materials as pseudocapacitors in a 3-electrode cell. (a) CVs of r-CMO performed at multiple scan rates over a 1 V window. (b) CVs of r-CMO RP performed at multiple scan rates over a 1 V window. (c) CVs of $\text{SrFeO}_{2.5}$ (SFO) performed at multiple scan rates over a 1 V window. (d) Capacitances of all four CMO materials at multiple scan rates. All CVs were performed in Ar-saturated 1 M KOH and performed in triplicate.

Effects of Oxygen Diffusion on Pseudocapacitance

The results presented above clearly show that oxygen vacancies play a crucial role in charge storage via anion intercalation as the capacitances for both the perovskite and RP materials increased dramatically after reduction, consistent with previous reports.¹⁵ However, if oxygen vacancy content were the only factor in

governing pseudocapacitive performance then we would not expect to see such a dramatic separation in performance between r-CMO and r-CMO RP at high scan rates as their oxygen vacancy contents are not a great deal different, and at low scan rates we would not see better performance from the RP materials versus the perovskites. Therefore, the differences between the two crystal structures themselves, specifically the incorporation of rock salt layers in the RP materials, must affect how oxide anions are shuttled into and out of the bulk material when surface hydroxide species are oxidized and the resulting oxygen anion is incorporated into the bulk.¹⁴

The dependence of peak current on scan rate (v) during cyclic voltammetry studies can be used to determine whether the process of charge storage through anion intercalation is controlled by charge transfer limitations or by oxide anion diffusion rates within the lattice. When the peak current densities are plotted versus scan rate, we find that the peak currents trend linearly as v for both anion intercalation and deintercalation in r-CMO, which indicates that charge transfer limitations are controlling the pseudocapacitive performance of the perovskite material. (Figure 3). For r-CMO RP, the peak currents are proportional to $v^{1/2}$ for anion intercalation and extraction, indicating that this process is diffusion limited.³²

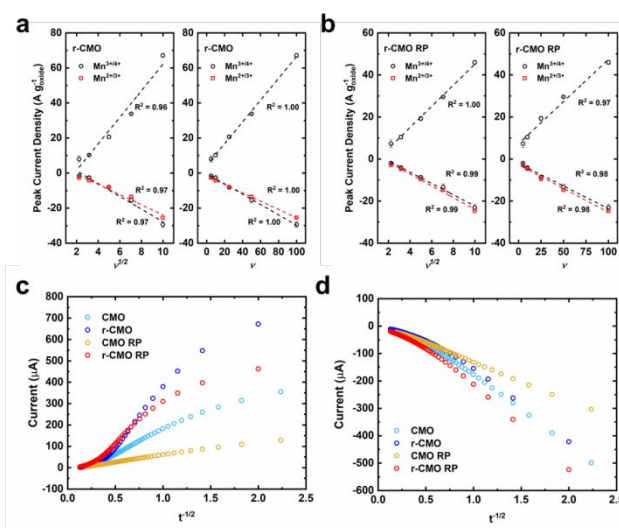


Figure 3: Effect of oxygen vacancies on bulk oxygen diffusion and charge storage. The dependence of the peak current densities on scan rate for (a) r-CMO and (b) r-CMO RP where the two cathodic peak current densities were measured at -0.1 V and -0.25 V . Oxygen diffusion rates were measured using a bounded diffusion model for (a) intercalation of oxygen and (b) deintercalation of oxygen from the bulk lattice for all four CMO materials.

To further probe the mechanism of charge storage the oxygen diffusion rates of both anion intercalation and deintercalation were measured for all four materials (Figure 3). These measurements are made by first performing three CVs at 10 mV s^{-1} to identify a stable peak position for the oxidation of Mn^{3+} to Mn^{4+} on the forward scan or for the reduction of Mn^{3+} to Mn^{2+} on the reverse scan, followed by chronoamperometry at a potential 50 mV more anodic (or cathodic) of these peaks to ensure a diffusion-limited process is taking place.

The current is plotted versus $t^{-1/2}$ and the linear portion of each curve is fitted. The time at $i = 0$ is extrapolated and used to calculate the diffusion rate using a bounded diffusion model as described elsewhere.^{33–35} Shown in Figure 3 and Table S1, reduction of both the perovskite and RP structures leads to concomitant increases in oxygen vacancy contents and oxygen diffusion rates with r-CMO and r-CMO RP displaying diffusion rates on the order of those seen for Li⁺ in Li ion battery materials^{36,37} and r-CMO displaying the overall highest measured oxygen intercalation diffusion rates ($2.64 \times 10^{-11} \pm 2.8 \times 10^{-12} \text{ cm}^2 \text{ s}^{-1}$). This is further evidenced by examining the CVs in Figure 2 for both the CMO and CMO RP materials in which at high scan rates the dominant cathodic peak is the reduction of Mn⁴⁺ to Mn³⁺ for both reduced materials indicating that intercalation and deintercalation are probably limited to a region near the particle surface, but as lower scan rates are used the Mn^{3+/2+} reduction peak contributes more to the overall discharge current, suggesting that increased amounts of oxide anions are diffusing into the bulk of the material, resulting in a more-reduced bulk structure. This lies in contrast to both unreduced samples in which both peaks contribute significantly to the overall charge stored at all scan rates used.

B-value analysis was performed on CVs taken at a variety of scan rates for r-CMO and r-CMO RP as described elsewhere¹⁵ to determine the fraction of current resulting from capacitive contributions versus the fraction of current measured that was due to diffusion-limited processes within the lattice. Figure 4 shows that for both r-CMO and r-CMO RP the amount of charge stored at high scan rates is due to significant contributions from both surface confined processes, such as double layer capacitance and deprotonation of surface hydroxide groups, and diffusion-limited intercalation of oxide anions into near-surface vacancy sites. At lower scan rates a larger portion of the charge stored is due to diffusion-limited oxide anion intercalation into and out of the bulk material.

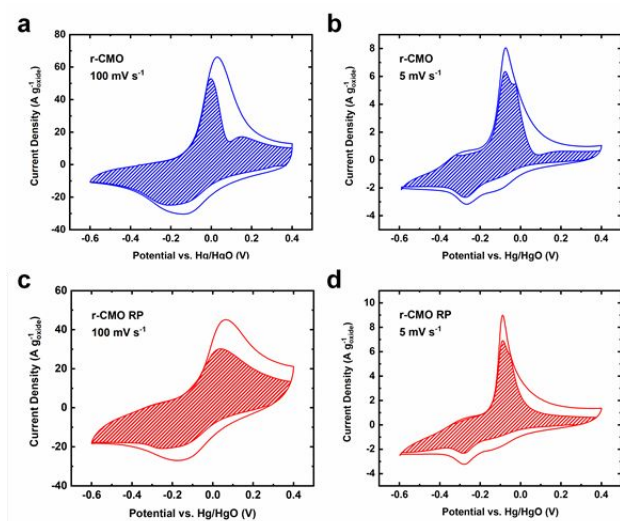


Figure 4. Capacitive components and oxygen vacancy trends. CVs in Ar-saturated 1 M KOH with the Faradaic current contributions shown in the shaded envelope for r-CMO at (a) 100 mV s⁻¹ and (b) 5 mV s⁻¹ and for r-CMO RP at (c) 100 mV s⁻¹ and (d) 5 mV s⁻¹.

We propose that there are three main factors contributing to the overall charge storage mechanism in the CMO materials: surface charge storage in the form of double layer capacitance and surface redox reactions, oxide anion intercalation into oxygen vacancy sites, and oxide anion storage in interstitial sites within the rock salt layers of the RP. At high scan rates, when shorter periods of time are spent at potentials capable of causing charge transfer, anion intercalation is confined to a region near the particle surface and in this scenario the oxygen vacancy content and number of available Mn redox sites play the most important role in pseudocapacitive performance. This finding is supported by both the measured capacitances as well as the increase in oxygen diffusion rates for both the perovskite and RP materials as more vacancies are introduced for oxide anions to diffuse into. Additionally, CMO RP displayed the slowest measured oxygen diffusion rate, demonstrating that oxygen diffusion through rock salt layers is slower than through perovskite layers and probably does not contribute significantly to charge storage at reduced time intervals. As slower scan rates are used, anion diffusion into and out of the bulk of the particle increases, aided by the fast oxygen diffusion rates described above. With the addition of the rock salt layers within the bulk, the RP can store oxide anions not only in vacancy sites within perovskite layers but in interstitial sites within the rock salt layers as well, resulting in superior performance. This hypothesis is corroborated by the measured capacitance of the unreduced RP sample that outperformed r-CMO at 5 mV s⁻¹ despite having far fewer oxygen vacancies and a slower measured oxygen diffusion rate. Furthermore, these trends in pseudocapacitance point to the stability of both crystal structures over short time periods in basic conditions. If either structure were rapidly decomposing into its constituent oxides then the perovskite materials would display significantly higher capacitances than their RP counterparts at all scan rates due to their greater Mn content.

Asymmetric Pseudocapacitor Cells

The reduced versions of the both the perovskite and Ruddlesden-Popper materials were investigated for their use in a two electrode, asymmetric pseudocapacitor cell in which the r-CMO and r-CMO RP materials were used as cathode materials while Brownmillerite SrFeO_{2.5} (SFO) was used as the anode material due to its exceptional ability to intercalate and deintercalate oxide anions and for its more-negative Fe redox potential (Figure 5).¹⁵ Three-electrode CVs for SFO can be seen in Figure 2 and a PXRD spectrum to confirm phase-purity of the material is presented in Figure S6. During charging of the cell the CMO materials are taken to potentials positive of the SFO and surface hydroxide groups are deprotonated to form O²⁻ that is intercalated into the CMO material while oxide anions are removed from SFO with the opposite process occurring during discharging. CVs of the two-electrode cell were used to determine the maximum potential window that could be used before water electrolysis would begin to occur during charging of the cell. As can be seen in Figure 5, after 1.65 V the current begins to increase independent of Mn redox events, signaling onset of water electrolysis and the edge of the potential window available for use. Thus, all galvanostatic charging

and discharging (GCD) experiments were performed over a 1.6 V potential window. The gravimetric capacitances calculated from the two-electrode CVs are shown in Figure S7.

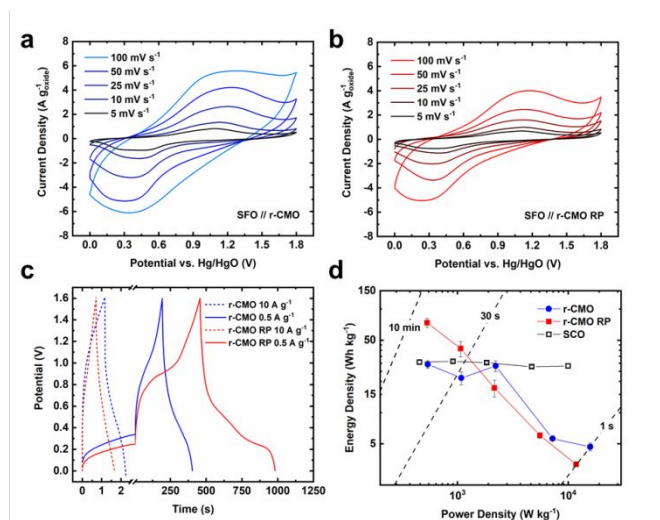


Figure 5. Two-electrode asymmetric cell experiments. CVs at various scan rates using $\text{SrFeO}_{2.5}$ as the anode material and either (a) r-CMO or (b) r-CMO RP as the cathode material. (c) GCD experiments were performed at current densities ranging from 10 A g^{-1} down to 0.5 A g^{-1} . (d) Ragone plot showing the energy density vs. power density at various discharge rates for cells containing both cathode materials as well as previously reported $\text{SrCoO}_{2.7}$.¹⁵ All measurements were performed in Ar-saturated 1 M KOH and in triplicate.

Galvanostatic charging and discharging experiments were then performed to more accurately reflect device operation conditions with the results of these experiments shown in Figure 5. Both CMO cathode materials resulted in cells that showed high energy and power densities, and the results directly reflect the trends seen in the three-electrode measurements discussed above. At high discharging rates, the cell in which r-CMO was used as the cathode outperformed the r-CMO RP material with r-CMO achieving an energy density of 5 Wh kg^{-1} at a power density of $15,800 \text{ W kg}^{-1}$ and r-CMO RP showing only 3 Wh kg^{-1} at a power density of $11,800 \text{ W kg}^{-1}$. At low current densities, however, anion intercalation into interstitial sites of the rock salt layer within the r-CMO RP structure dominates and leads to significantly higher performance (73 Wh kg^{-1} at 530 W kg^{-1}) than r-CMO (29 Wh kg^{-1} at 540 W kg^{-1}). The energy densities of both CMO materials at high power densities are much lower than $\text{SrCoO}_{2.7}$ (SCO) (28 Wh kg^{-1} at $10,000 \text{ W kg}^{-1}$) and other perovskite materials previously reported by our group that were employed in the same two-electrode cells using SFO as the anode.¹⁵ This is possibly due to the lower oxygen diffusion rates seen in the CMO materials versus previously reported perovskites that utilize La and Sr in the A-site and therefore have wider interstitial sites through which oxygen can diffuse more readily. Additionally, each electron removed from Mn during discharging has less energy than those removed from SCO due to the more anodic potential at which these redox reactions occur in SCO that results in a larger potential window of the SFO//SCO cell.

However, at slower charging and discharging rates the power densities of CMO materials compare much more favorably with SCO (31 Wh kg^{-1} at 450 W kg^{-1}) and r-CMO RP functions to achieve a much higher energy density at similar power densities when slower discharge rates are used due to the ability to intercalate anions into interstitial sites of the rock salt layers within r-CMO RP.

Conclusions

The electrochemical pseudocapacitance of CaMnO_{3-x} and $\text{Ca}_2\text{MnO}_4-x$ materials have been studied via potentiodynamic measurements. Reduced versions of both CMO materials that were formed by annealing in a reducing atmosphere displayed greater pseudocapacitive performance than their unreduced counterparts, verifying that greater oxygen vacancy concentrations within the bulk of these materials increases their ability to store charge via anion intercalation. Furthermore, we demonstrate how a governing descriptor for pseudocapacitive performance changes from a dependence on the number of surface redox sites and oxygen vacancies at high scan rates to a dependence on facile oxygen diffusion through the bulk lattice and the ability to intercalate oxide anions into the interstitial sites of the rock salt layers of the Ruddlesden-Popper crystal structure at slow scan rates. Finally, we demonstrate how both materials maintain the impressive redox pseudocapacitive performance observed in the three-electrode cell when used in an asymmetric, 2-electrode pseudocapacitor configuration and how these measurements verify the trends described above.

The conclusions section should come in this section at the end of the article, before the acknowledgements.

Conflicts of interest

There are no conflicts to declare.

Acknowledgements

Financial support for this work was provided by the R. A. Welch Foundation (grants F-1529 and F-1319). The Kratos XPS was funded by the NSF under grant CHE-0618242. R.P.F. performed the synthesis, X-ray diffraction, iodometric titrations and electrochemical characterization. J.P. performed XPS analysis. C.T.A. provided reference electrochemical data and intellectual contributions to this work. R.P.F., C.T.A., K.P.J. and K.J.S. aided in construction of the manuscript.

References

1. Miller, J. R. & Simon, P. Electrochemical Capacitors for Energy Management. *Science* **321**, 651–652 (2008).
2. Zhang, L. L., Zhou, R. & Zhao, X. S. Graphene-based materials as supercapacitor electrodes. *J. Mater. Chem.* **20**, 5983–5992 (2010).
3. Conway, B. E. *Electrochemical Supercapacitors*. (Springer, 1999).

- Wang, F. *et al.* Electrode materials for aqueous asymmetric supercapacitors. *RSC Adv.* **3**, 13059–13084 (2013).
- Simon, P. & Gogotsi, Y. Materials for electrochemical capacitors. *Nature Materials* **7**, 845–854 (2008).
- Wang, G., Zhang, L. & Zhang, J. A review of electrode materials for electrochemical supercapacitors. *Chem. Soc. Rev.* **41**, 797–828 (2012).
- Gu, J. *et al.* Asymmetric capacitors based on TiO₂ and mesoporous MnO₂ electrodes using neutral aqueous electrolyte. *J. Nanopart. Res.* **19**, 322 (2017).
- Forslund, R. P. *et al.* Nanostructured LaNiO₃ Perovskite Electrocatalyst for Enhanced Urea Oxidation. *ACS Catal.* **6**, 5044–5051 (2016).
- Wang, H., Casalongue, H. S., Liang, Y. & Dai, H. Ni(OH)₂ Nanoplates Grown on Graphene as Advanced Electrochemical Pseudocapacitor Materials. *J. Am. Chem. Soc.* **132**, 7472–7477 (2010).
- Zolfaghari, A., Chayer, M. & Jerkiewicz, G. Energetics of the Underpotential Deposition of Hydrogen on Platinum Electrodes I. Absence of Coadsorbed Species. *J. Electrochem. Soc.* **144**, 3034–3041 (1997).
- Marković, N. M., Lucas, C. A., Gasteiger, H. A. & Ross, P. N. Bromide adsorption on Pt(100): rotating ring-Pt(100) disk electrode and surface X-ray scattering measurements. *Surface Science* **365**, 229–240 (1996).
- Brezesinski, K. *et al.* Pseudocapacitive contributions to charge storage in highly ordered mesoporous group V transition metal oxides with iso-oriented layered nanocrystalline domains. *J. Am. Chem. Soc.* **132**, 6982–6990 (2010).
- Brezesinski, T., Wang, J., Tolbert, S. H. & Dunn, B. Ordered mesoporous α -MoO₃ with iso-oriented nanocrystalline walls for thin-film pseudocapacitors. *Nature Materials* **9**, 146–151 (2010).
- Mefford, J. T., Hardin, W. G., Dai, S., Johnston, K. P. & Stevenson, K. J. Anion charge storage through oxygen intercalation in LaMnO₃ perovskite pseudocapacitor electrodes. *Nat. Mater.* **13**, 726–732 (2014).
- Alexander, C. T. *et al.* Anion-Based Pseudocapacitance of the Perovskite Library La_{1-x}Sr_xBO_{3- δ} (B = Fe, Mn, Co). *ACS Appl. Mater. Interfaces* **11**, 5084–5094 (2019).
- Forslund, R. P. *et al.* Exceptional electrocatalytic oxygen evolution via tunable charge transfer interactions in La_{0.5}Sr_{1.5}Ni_{1-x}Fe_xO_{4 \pm δ} Ruddlesden-Popper oxides. *Nature Communications* **9**, 3150 (2018).
- Forslund, R. P., Alexander, C. T., Abakumov, A. M., Johnston, K. P. & Stevenson, K. J. Enhanced Electrocatalytic Activities by Substitutional Tuning of Nickel-Based Ruddlesden-Popper Catalysts for the Oxidation of Urea and Small Alcohols. *ACS Catal.* **9**, 2664–2673 (2019).
- Liu, Y., Dinh, J., Tade, M. O. & Shao, Z. Design of Perovskite Oxides as Anion-Intercalation-Type Electrodes for Supercapacitors: Cation Leaching Effect. *ACS Appl. Mater. Interfaces* **8**, 23774–23783 (2016).
- Che, W. *et al.* Perovskite LaNiO_{3- δ} oxide as an anion-intercalated pseudocapacitor electrode. *J. Alloys Compd.* **731**, 381–388 (2018).
- Lang, X., Mo, H., Hu, X. & Tian, H. Supercapacitor performance of perovskite La_{1-x}Sr_xMnO₃. *Dalton Trans.* **46**, 13720–13730 (2017).
- Ali, G. A. M., Wahba, O. A. G., Hassan, A. M., Fouad, O. A. & Feng Chong, K. Calcium-based nanosized mixed metal oxides for supercapacitor application. *Ceram. Int.* **41**, 8230–8234 (2015).
- Mo, H. *et al.* Influence of calcium doping on performance of LaMnO₃ supercapacitors. *Ceram. Int.* **44**, 9733–9741 (2018).
- Poepelmeier, K. R., Leonowicz, M. E. & Longo, J. M. CaMnO_{2.5} and Ca₂MnO_{3.5}: New oxygen-defect perovskite-type oxides. *Journal of Solid State Chemistry* **44**, 89–98 (1982).
- Poepelmeier, K. R., Leonowicz, M. E., Scanlon, J. C., Longo, J. M. & Yelon, W. B. Structure determination of CaMnO₃ and CaMnO_{2.5} by X-ray and neutron methods. *J. Solid State Chem.* **45**, 71–79 (1982).
- Du, J. *et al.* Nonstoichiometric Perovskite CaMnO_{3- δ} for Oxygen Electrocatalysis with High Activity. *Inorg. Chem.* **53**, 9106–9114 (2014).
- Gorlin, Y. & Jaramillo, T. F. A Bifunctional Nonprecious Metal Catalyst for Oxygen Reduction and Water Oxidation. *J. Am. Chem. Soc.* **132**, 13612–13614 (2010).
- Han, X., Hu, Y., Yang, J., Cheng, F. & Chen, J. Porous perovskite CaMnO₃ as an electrocatalyst for rechargeable Li–O₂ batteries. *Chem. Commun.* **50**, 1497–1499 (2014).
- Kim, J., Chen, X., Pan, Y.-T., Shih, P.-C. & Yang, H. W-Doped CaMnO_{2.5} and CaMnO₃ Electrocatalysts for Enhanced Performance in Oxygen Evolution and Reduction Reactions. *J. Electrochem. Soc.* **164**, F1074–F1080 (2017).
- Peng, S. *et al.* Electronic and Defective Engineering of Electrospun CaMnO₃ Nanotubes for Enhanced Oxygen Electrocatalysis in Rechargeable Zinc–Air Batteries. *Adv. Energy Mater.* **8**, 1800612 (2018).
- Biesinger, M. C. *et al.* Resolving surface chemical states in XPS analysis of first row transition metals, oxides and hydroxides: Cr, Mn, Fe, Co and Ni. *Appl. Surf. Sci.* **257**, 2717–2730 (2011).
- Bakken, E. *et al.* Entropy of oxidation and redox energetics of CaMnO_{3- δ} - ScienceDirect. *Solid State Ionics* **176**, 2261–2267 (2005).
- Bard, A. J. & Faulkner, L. R. *Electrochemical Methods: Fundamentals and Applications*. (Wiley, 2000).
- Van Buren, F. R., Broers, G. H. J., Bouman, A. J. & Boesveld, C. An electrochemical method for the determination of oxygen ion diffusion coefficients in La_{1-x}Sr_xCoO_{3-y} compounds. *J. Electroanal. Chem. Interfacial Electrochem.* **87**, 389–394 (1978).
- Van Buren, F. R., Broers, G. H. J., Bouman, A. J. & Boesveld, C. The electrochemical determination of oxygen ion diffusion coefficients in La_{0.50}Sr_{0.50}CoO_{3-y}: Experimental results and related properties. *J. Electroanal. Chem. Interfacial Electrochem.* **88**, 353–361 (1978).
- Kobussen, A. G. C., van Buren, F. R. & Broers, G. H. J. The influence of the particle size distribution on the measurement of oxygen ion diffusion coefficients in La_{0.50}Sr_{0.50}CoO_{3-y}. *J. Electroanal. Chem. Interfacial Electrochem.* **91**, 211–217 (1978).
- Mizushima, K., Jones, P. C., Wiseman, P. J. & Goodenough, J. B. Li_xCoO₂ (0 < x < 1): A new cathode material for batteries of high energy density. *Materials Research Bulletin* **15**, 783–789 (1980).
- Yu, P., Popov, B. N., Ritter, J. A. & White, R. E. Determination of the Lithium Ion Diffusion Coefficient in Graphite. *J. Electrochem. Soc.* **146**, 8–14 (1999).